Theory of necking localization in unconstrained electromagnetic expansion of thin sheets

J.D. Thomas, N. Triantafyllidis *

The University of Michigan, Aerospace Engineering Department, Ann Arbor, MI 48109-2140, USA

Abstract

Certain sheet metal alloys of industrial interest show a significant increase in ductility, over conventional forming methods, when high speed electromagnetic processes are used. The present work models the necking localization of a metal sheet during an electromagnetic process and examines the factors that influence this process. A Marciniak–Kuczynski "weak band" model is used to predict the onset of necking of a thin sheet under plane stress, an idealization of the local conditions in a thin sheet subjected to unconstrained electromagnetic loading. It is found that electromagnetic forming (EMF) increases ductility over quasistatic techniques due to the material's strain-rate sensitivity, with ductility increasing monotonically with applied strain rates. The electric current also increases onset of necking strains, but the details depend on thermal sensitivity and temperature-dependence of the strain-rate sensitivity exponent. Given the insensitivity of the results to actual strain profiles, this local type analysis provides a useful tool that can be used for ductility predictions involving EMF processes.
© 2007 Elsevier Ltd. All rights reserved.

Keywords: Electromagnetic forming; Ductility; High strain-rate; Thermoplasticity; Viscoplastic

1. Introduction

Electromagnetic forming (EMF) is a cost-effective and flexible manufacturing technique for sheet metal forming. It consists of connecting an actuator (typically a copper wire solenoid) to a high energy capacitor equipped with fast action switches. When the capacitor is discharged, the large transient current that goes through the actuator generates by induction strong eddy currents in the nearby metallic workpiece. The presence of these induced currents, inside the magnetic field generated by the currents of the actuator, results in Lorentz body forces in the workpiece which are responsible for its plastic deformation.

The EMF techniques are popular in the aerospace and automotive industries because of several advantages they hold over conventional forming techniques. These advantages are: process repeatability and flexibility (due to its electric nature, energy input can be easily and accurately adjusted), low cost single side tooling (thus

---

reducing need for lubrication and tool marks) and high speed (typical process duration is on the order of 50 μs). The most important advantage – and the main reason for the recent interest in EMF – is the resulting significant increase in ductility observed in certain metals, with aluminum featuring preeminently among them. Experimental results by Balanethiram and Daehn (1992, 1994) with die impact EMF show dramatic increases (compared to conventional forming) in the ductility of AA6061-T4. Their work shows that electromagnetically formed aluminum alloys are potentially and significantly more ductile than conventionally formed steel alloys (DFQ steel, which is about twice as ductile as conventionally formed AA6061-T4). A key ingredient in this ductility increase is the strain-rate sensitivity of the material's constitutive response, as explained by Hutchinson and Neale (1977). A detailed theoretical explanation of this observed increase in formability, based on fully coupled electromagnetic and thermomechanical modeling of the free expansion of an electromagnetically loaded ring, was recently provided by Triantafyllidis and Waldenmyer (2004).

In order to quantify the ductility of sheet metal a key concept is that of a forming limit diagram (FLD), according to which a thin sheet (stress-free in the thickness direction) is subjected to proportional in-plane straining until the onset of localization. Typical examples of an EMF process with these (approximate) forming conditions are circular plate expansion (loaded by a flat coil parallel to the plate) and axisymmetric tube bulging (loaded by a cylindrical coil coaxial with the tube). Fig. 1 shows a freely, electromagnetically expanded tube at the end of deformation with necking zones. There is a voluminous mechanics literature going back to the early 1970's addressing the choice of localization criterion as well as the influence of the constitutive properties on the onset of localization prediction. However, all of these investigations address a mechanical deformation phenomenon but none – to the best of our knowledge – addresses the coupled electromagnetic-thermomechanical localization problem that occurs with electromagnetic forming of sheet metal, thus motivating the present work.

More specifically, the goals of this investigation are: (i) the theoretical formulation for the onset of necking in an electromagnetically loaded thin sheet, i.e. subjected simultaneously to in-plane stresses and electric currents, and (ii) the influence of the process characteristics and constitutive law on the resulting necking predictions, i.e. how the various aspects of the EMF process and thermoviscoplastic constitutive law influence the FLD. The analysis here is general for EMF process ductility calculations, but for reasonable data the simulation is based on aluminum alloys and axisymmetric processes. Since the constitutive choice is of paramount importance for the FLD predictions, the bulk of the results pertain to investigating how different parameters of the adopted law (hardening, rate and thermal sensitivity as well as yield surface shape) affect onset of necking predictions.
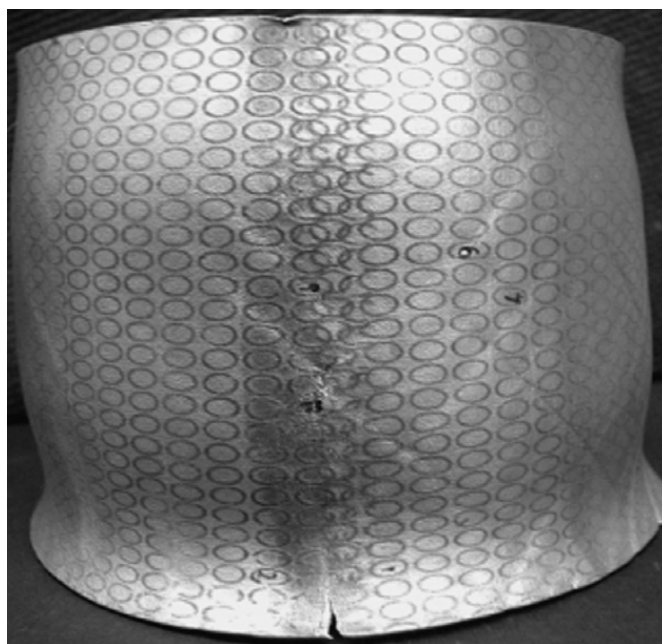

Fig. 1. Onset of necking in a freely, electromagnetically expanded tube (courtesy of Professor Glenn Daehn, The Ohio State University).
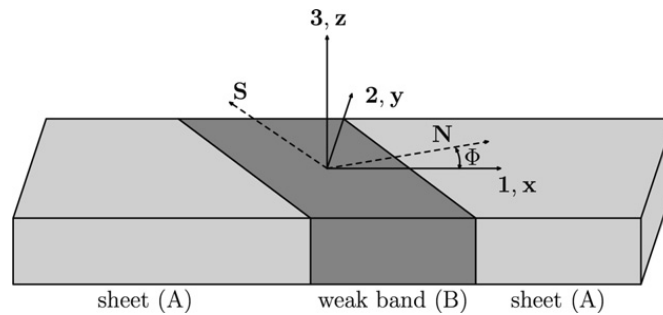
Fig. 2. Reference configuration geometry of the weak band.

The presentation is organized as follows: Section 2 presents the theoretical formulation of the onset of necking problem in a finitely strained thin sheet under combined in-plane stresses and electric currents. The analysis is based on a Marciniak–Kuczynski "weak band" model using a full Lagrangian formulation. The same section deals with the most general form of the thermoviscoplastic constitutive law and explains the choice for the strain and current density profiles. In Section 3, following a brief explanation of the numerical algorithm adopted for solving the problem's ordinary differential equations (ODEs), are presented and discussed the results of the investigation, while Section 4 concludes the work. The important issue of choice for the onset of necking criterion is presented in detail and justified in Appendix A, where the weak band imperfection criterion is compared to a linearized stability criterion that is independent of imperfection size.

2. Problem formulation

As discussed in Section 1, a weak band analysis for the localization of deformation is used to analyze the onset of necking in an unconstrained, electromagnetically expanded axisymmetric tube or plate, modeled as a biaxially stretched sheet subjected to electric currents. The governing equations for the mechanical and electrical field quantities in the localized deformation zone are followed by the presentation of the rate and temperature-dependent constitutive models for the sheet. The adopted strain and electric current profiles for modeling the EMF process complete the simulation description.

2.1. Localization zone analysis

Fig. 2 shows a thin sheet under plane stress conditions, an idealization of a small portion of a tube or plate sheet, thus ignoring curvature effects. Inertia effects are also ignored in the present analysis, and the tube or plate hoop direction and the 1-direction in Fig. 2 are taken coincident. Localized deformation is assumed to occur in a narrow band (B) with normal direction $N = i \cos \Phi + j \sin \Phi$ and tangent $S = -i \sin \Phi + j \cos \Phi$. These are the reference configuration directions, while the corresponding current configuration quantities are denoted by n, s and ϕ. An initial imperfection differentiates the band and sheet and is implemented as either a material parameter or geometric (thickness) discontinuity in the reference configuration properties. With this model in place, one endeavors to calculate the deformation gradient F^B, stress σ^B, current j^B, temperature θ^B and internal variable (plastic strain) ϵ_B^p inside the band from their counterpart quantities outside the band (F^A, σ^A, j^A, θ^A and ϵ_A^p).

The large deformations inherent in this problem lead naturally to a full Lagrangian (reference configuration) formulation. A current configuration formulation could have been chosen, but the Lagrangian formulation consistently accounts for the complex large deformation kinematics, reducing the likelihood of errors in the analysis. Mechanical considerations require that displacement and traction be preserved across the band. More specifically displacement continuity across the band dictates[1]

---

[1] Here and subsequently Greek indexes range from 1 to 2 while Latin indexes range from 1 to 3. Einstein's summation convention over repeated indexes is implied, unless specified otherwise.

$$\left[F_{\alpha\beta}^B - F_{\alpha\beta}^A\right]S_\beta = 0, \tag{2.1}$$

and traction continuity requires

$$N_\alpha\left[\Pi_{\alpha\beta}^B - \Pi_{\alpha\beta}^A\right] = 0, \tag{2.2}$$

where the first Piola–Kirchhoff (P–K) stress $\mathbf{\Pi}$ is expressed in terms of the Cauchy stress as

$$\Pi_{ij} = \det(\mathbf{F})\left[F_{ik}^{-1}\sigma_{kj}\right]. \tag{2.3}$$

Electrical considerations require that the electric current and tangential component of the electromotive force must be preserved across the band. From current continuity one has

$$N_\alpha\left[J_\alpha^B - J_\alpha^A\right] = 0, \tag{2.4}$$

where the electric current density vector in the reference configuration $\mathbf{J}$ is related to $\mathbf{j}$, its counterpart in the current configuration, by

$$J_i = \det(\mathbf{F})\left[F_{ik}^{-1}j_k\right]. \tag{2.5}$$

Faraday's induction law requires that the tangential component of the electromotive force in the reference configuration $\mathbf{E}$ be preserved, which dictates

$$S_\alpha\left[E_\alpha^B - E_\alpha^A\right] = 0, \tag{2.6}$$

where the reference configuration electromotive force $\mathbf{E}$ is related to its current configuration counterpart $\mathbf{e}$ by

$$E_i = e_k F_{ki}. \tag{2.7}$$

Finally, assuming adiabatic heating both outside (A) and inside (B) the weak band (thus the various field quantities need not be indexed), energy conservation (per unit current volume) dictates

$$\mu c_{\mathrm{p}}\dot{\theta} = \chi\sigma_{\mathrm{e}}\dot{\epsilon}^{\mathrm{p}} + e_i j_i, \tag{2.8}$$

where μ is the mass density, c_{p} is the specific heat, $\dot{\theta}$ is the rate of change of the temperature, χ ($0 < \chi < 1$) is the plastic work conversion factor and $\sigma_{\mathrm{e}}\dot{\epsilon}^{\mathrm{p}}$ is the plastic dissipation (σ_{e} is the equivalent Cauchy stress and ϵ^{p} is the plastic strain).

2.2. Constitutive response

Due to the electromagnetic nature of the forming process, the simulation requires two sets of constitutive equations: one for the mechanical response and one for the electrical response.

2.2.1. Mechanical constitutive law

An EMF process imposes high strain rates and high temperatures on the workpiece, thus requiring a temperature-dependent viscoplastic constitutive law, which can be described by

$$\mathring{\sigma}_{ij} = \mathcal{L}_{ijkl}^{\mathrm{e}} D_{kl}^{\mathrm{e}}, \tag{2.9}$$

where $\mathring{\sigma}_{ij}$ denotes the convected rate of Cauchy stress, $\mathcal{L}_{ijkl}^{\mathrm{e}}$ are the solid's elastic moduli and D_{ij}^{e} are the elastic components of the strain-rate tensor. The frame-invariant stress rate $\mathring{\sigma}_{ij}$ is given in terms of the stress rate $\dot{\sigma}_{ij}$ by

$$\mathring{\sigma}_{ij} = \dot{\sigma}_{ij} + L_{ki}\sigma_{kj} + \sigma_{ik}L_{kj}, \tag{2.10}$$

where L_{ij} is the solid's velocity gradient. Note that the choice of the convected rate of stress is arbitrary.

The strain rate may be additively decomposed into an elastic $\mathbf{D}^{\mathrm{e}}$, a plastic $\mathbf{D}^{\mathrm{p}}$ and a thermal $\mathbf{D}^{\theta}$ part, as follows:

$$D_{ij} = D_{ij}^{\mathrm{e}} + D_{ij}^{\mathrm{p}} + D_{ij}^{\theta}. \tag{2.11}$$

The plastic part of the strain rate for a viscoplastic solid which is described in terms of only one internal variable ϵ^{p} – the accumulated plastic strain – is

$$D_{ij}^{\mathrm{p}} = \dot{\epsilon}^{\mathrm{p}} \frac{\partial \sigma_{\mathrm{e}}}{\partial \sigma_{ij}}, \qquad (2.12)$$

while the thermal part of the strain rate is

$$D_{ij}^{\theta} = \eta \dot{\theta} \delta_{ij}, \qquad (2.13)$$

where η is the thermal expansion coefficient. The internal variable ϵ^{p} determines the size of the material's current yield surface, which is characterized by the equivalent stress σ_{e}, and the relation between ϵ^{p} and the solid's quasistatic uniaxial response $\sigma = g(\epsilon^{p}, \theta)$ is

$$\dot{\epsilon}^{\mathrm{p}} = \dot{\epsilon}_0^{\mathrm{p}} \left[\left(\frac{\sigma_{\mathrm{e}}(\sigma_{ij})}{g(\epsilon^{\mathrm{p}}, \theta)} \right)^{1/m(\theta)} - 1 \right], \qquad (2.14)$$

where $m(\theta)$ is the solid's rate-sensitivity exponent that is (in general) a function of temperature and $\dot{\epsilon}_0^{\mathrm{p}}$ is a material constant. Expressions that are based on experiments will be given subsequently for $\sigma_{\mathrm{e}}(\sigma_{ij})$ and $g(\epsilon^{\mathrm{p}}, \theta)$.

Attention is now turned to the required kinematical relations. The components of the strain rate D_{ij} and velocity gradient L_{ij} are given in terms of the deformation gradient and its rate by

$$D_{ij} = \frac{1}{2} \left(L_{ij} + L_{ji} \right), \quad L_{ij} = \dot{F}_{ik} F_{kj}^{-1}. \qquad (2.15)$$

In the preceding equations the constitutive relations are presented in a general three dimensional form. For the EMF tube or circular disk bulging simulation, a state of plane stress is assumed. Consequently, only in-plane deformations are considered, and in view of transverse isotropy of the sheet one has

$$F_{\alpha 3} = F_{3\alpha} = 0, \qquad (2.16)$$

while the state of plane stress dictates

$$\sigma_{i3} = 0. \qquad (2.17)$$

The plane stress version of the constitutive equation (2.9) is thus expressed as

$$\overset{\circ}{\sigma}_{\alpha\beta} = \hat{\mathcal{L}}_{\alpha\beta\gamma\delta}^{\mathrm{e}} D_{\gamma\delta}^{\mathrm{e}}, \qquad (2.18)$$

where the plane stress elastic moduli $\hat{\mathcal{L}}_{\alpha\beta\gamma\delta}^{\mathrm{e}}$ and the full three-dimensional moduli are related by

$$\hat{\mathcal{L}}_{\alpha\beta\gamma\delta}^{\mathrm{e}} = \mathcal{L}_{\alpha\beta\gamma\delta}^{\mathrm{e}} - \mathcal{L}_{\alpha\beta33}^{\mathrm{e}} (\mathcal{L}_{3333}^{\mathrm{e}})^{-1} \mathcal{L}_{33\gamma\delta}^{\mathrm{e}}. \qquad (2.19)$$

To complete this temperature-dependent, viscoplastic model two experimentally based elements are necessary: the rate-independent uniaxial response $\sigma = g(\epsilon^{\mathrm{p}}, \theta)$ and the yield surface $\sigma_{\mathrm{e}}(\sigma_{ij})$.

The experimentally motivated (see Yadav et al., 2001) rate-independent uniaxial response employed here is given by

$$g(\epsilon^{\mathrm{p}}, \theta) = \sigma_y \left[1 + \frac{\epsilon^{\mathrm{p}}}{\epsilon_y} \right]^n \left[1 - \left(\frac{\theta - \theta_0}{\theta_m - \theta_0} \right)^{\alpha} \right], \qquad (2.20)$$

where σ_y is the yield stress, $\epsilon_y = \sigma_y/E$ is the yield strain, n is the hardening exponent, θ_m is the melting temperature, θ_0 is the reference temperature and α is the thermal sensitivity exponent.

The mechanical constitutive equations are completed with the yield surface description. Three different yield surfaces are considered in this work. The first is the familiar von Mises (isotropic, quadratic) yield surface, included for comparison purposes. The second is an isotropic, nonquadratic yield surface. These two models are appropriate for isotropic materials that do not exhibit the Bauschinger effect, i.e. materials that exhibit no difference between their tensile and compressive responses, and both are described by

$$\sigma_{\mathrm{e}} = \left[\left(|\sigma_1 - \sigma_2|^{\beta} + |\sigma_2 - \sigma_3|^{\beta} + |\sigma_3 - \sigma_1|^{\beta} \right)/2 \right]^{1/\beta}, \qquad (2.21)$$

where β is a coefficient determined by the yield surface and material type and σ_i are the principal values of the Cauchy stress tensor. The von Mises yield surface requires $\beta = 2$, and for the nonquadratic surface, experimental evidence suggests $\beta = 8$ for aluminum (see Barlat et al., 1997b and references cited therein).

The third yield surface considered is an anisotropic nonquadratic yield surface Yld94, proposed for aluminum alloys by Barlat et al. (1997a). It is described by

$$\sigma_e = \left[\left(\alpha_x |s_2 - s_3|^\beta + \alpha_y |s_3 - s_1|^\beta + \alpha_z |s_1 - s_2|^\beta \right)/2 \right]^{1/\beta}, \tag{2.22}$$

where again $\beta = 8$ for aluminum. Moreover, the auxiliary isotropic stress $\mathbf{s}$ (with principal values s_1, s_2, s_3) is related to the actual Cauchy stress $\boldsymbol{\sigma}$ by

$$s_{ij} = L_{ijkl}\sigma_{kl}, \quad \mathbf{L} = \begin{bmatrix} \frac{1}{3}(c_2 + c_3) & -\frac{1}{3}(c_3) & -\frac{1}{3}(c_2) & 0 & 0 & 0 \\ -\frac{1}{3}(c_3) & \frac{1}{3}(c_3 + c_1) & -\frac{1}{3}(c_1) & 0 & 0 & 0 \\ -\frac{1}{3}(c_2) & -\frac{1}{3}(c_1) & \frac{1}{3}(c_2 + c_1) & 0 & 0 & 0 \\ 0 & 0 & 0 & c_4 & 0 & 0 \\ 0 & 0 & 0 & 0 & c_5 & 0 \\ 0 & 0 & 0 & 0 & 0 & c_6 \end{bmatrix}. \tag{2.23}$$

The experimentally determined parameters $\alpha_x, \alpha_y, \alpha_z, c_1, c_2, c_3, c_4, c_5, c_6$ which determine the sheet's anisotropy are taken here as constants. It should be mentioned in Yld94 the parameters $\alpha_x, \alpha_y, \alpha_z$ are more generally functions of the stress state. The axes of material anisotropy are taken to coincide with the axes in Fig. 2 (i.e. the rolling direction is aligned with the 1-direction), so the stress dependence of $\alpha_x, \alpha_y, \alpha_z$ is actuated only for strain paths with one positive and one negative principal strain (Barlat et al., 1997b). However, for these paths the influence of the yield surface anisotropy on the localization strain is not found to be significant (see also Butuc et al., 2003), thus justifying our choice of using constant $\alpha_x, \alpha_y, \alpha_z$.

2.2.2. Electrical constitutive law

In addition to the mechanical an electrical constitutive response of the material is required. Here for simplicity an isotropic Ohm's law is assumed,

$$e_\alpha = r(\theta) j_\alpha, \tag{2.24}$$

where $r(\theta)$ is the resistivity of the isotropic sheet that is in general a function of temperature. This relation in addition to Eq. (2.7) allows Eq. (2.6) to be utilized (in addition to Eq. (2.4)) to find the currents j^B in the weak band.

One now has in Eqs. (2.9)–(2.24) a complete description of the solid's constitutive response, where the necessary material constants are determined from experiments. An account of the material constant selection is given below.

2.3. Material parameter selection

Finding an alloy where all the relevant material parameters for the viscoplastic model in Sections 2.1 and 2.2 have been determined experimentally is a rather formidable task. A combination of AA6061-T6 and AA6016-T4 parameters seems the best available option for conducting a meaningful simulation. Constitutive parameters for AA6061-T6 are given by Yadav et al. (2001), based on experimental results by Yadav et al. (1995), and are presented in Table 1.

Additional material parameters are required to implement Eqs. (2.8) and (2.12). These parameters can be found from standard tables for aluminum (see also Triantafyllidis and Waldenmyer, 2004) and are presented in Table 2.

Values for the parameters describing the alloy's yield surface are also needed. Unfortunately, there is no information in the open literature regarding values for these parameters for AA6061-T6. This forces a compromise to be made, and these parameters are obtained from the closest available material data. Butuc et al.

Table 1
AA6061-T6 Uniaxial response parameter values (Yadav et al., 2001)

$\sigma_y = 276$ MPa	$E = 69$ GPa	$\epsilon_y = \sigma_y/E$
$n = 0.0741$	$m = 0.0870$	$\alpha = 0.5$
$\dot{\epsilon}_0^p = 1000$ s^{-1}	$\theta_0 = 298$ K	$\theta_m = 853$ K

Table 2
AA6061-T6 Material parameter values (Triantafyllidis and Waldenmyer, 2004)

$\mu = 2700$ kg/m^3	$c_p = 896$ J/kg K	
$\chi = 0.9$	$r_0 = 2.65 \times 10^{-8}$ Ωm	$\eta = 2.3 \times 10^{-5}$ 1/K

(2003) provide these data, which pertain to AA6016-T4, and the values for the corresponding parameters are given in Table 3.

Triggering localized deformation requires an initial imperfection in the weak band, according to Marciniak and Kuczynski (1967) who first introduced this concept in predicting forming limit diagrams in the tensile region. Initially a thickness imperfection distinguished the weak band (e.g. Marciniak and Kuczynski, 1967), but imperfections in other material parameters were subsequently shown to be useful in predicting forming limits (e.g. Needleman and Triantafyllidis (1978)). Results of this method are sensitive to the magnitude of the imperfection. Alternative methods that do not utilize an imperfection have been proposed for rate-independent solids by Stören and Rice (1975) and for rate-dependent solids by Triantafyllidis et al. (1997). Unfortunately, the deformation theory approach proposed by Stören and Rice (1975) cannot be generalized for viscoplastic solids, while the perturbation method introduced by Triantafyllidis et al. (1997) produces unreasonable results for tensile loading (see Appendix A).

For reasons discussed in detail in Appendix A, the weak band method of Marciniak and Kuczynski (1967) has been adopted. A weakness in the yield stress σ_y is implemented using the imperfection parameter ξ such that $\sigma_y^B = (1 - \xi)\sigma_y^A$. In choosing a value for ξ simulated quasistatic (rate-independent, isothermal) forming limit curves using proportional straining paths and varying ξ values are considered. The sensitivity of these curves to ξ is most pronounced for biaxial stretching strain paths ($\epsilon_1 > 0$, $\epsilon_2 > 0$), while strain paths with one positive and one nonpositive principal strain ($\epsilon_1 > 0$, $\epsilon_2 \leqslant 0$) show relatively little dependence on the value of the imperfection parameter. The resulting onset of necking curves are compared with the experimental quasistatic forming limit diagram for AA6061-T6, presented by LeRoy and Embury (1978). Requiring a value for ξ that gives the best overall agreement between simulated and measured forming limit curves resulted in the present choice of $\xi = 0.001$.

The issue of a temperature-dependent strain-rate sensitivity m needs also to be addressed. The constant value for m given in Table 1 does give a reasonable correlation with experimental constitutive data (Yadav et al., 2001), and this value will be used in the "base case" set of parameters. However, there is compelling evidence (see Krajewski, 2005; Ogawa, 2001) that the strain-rate sensitivity is an increasing function of temperature, $m(\theta)$.

To obtain a reasonable estimate for $m(\theta)$, the work of Tirupataiah and Sundararajan (1994) and Ogawa (2001) is used. Tirupataiah and Sundararajan (1994) show a material-dependent transition strain rate between low strain-rate sensitivity and high strain-rate sensitivity. For aluminum with properties similar to AA6061-T6, the transition occurs at or below 100 s^{-1}; typical EMF strain rates are well above this. Thus, only data for strain rates above 100 s^{-1} are appropriate to fit a temperature-dependent strain-rate sensitivity for EMF processes. Ogawa (2001) provides stress versus strain rate data on AA6061-T6 at 5% strain (or 6%, noted appro-

Table 3
AA6016-T4 Yield surface parameter values (Butuc et al., 2003)

$\alpha_x = 2.0$	$\alpha_y = 3.5$	$\alpha_z = 1.0$	
$c_1 = 1.0474$	$c_2 = 0.7752$	$c_3 = 1.0724$	$c_6 = 0.9288$

priately in the paper) for temperatures ranging from 77 to 473 K and strain rates up to $1.5 \times 10^5 \text{ s}^{-1}$. Eqs. (2.14) and (2.20) are used to find m at the different temperatures (m is assumed independent of strain rate); the quasistatic flow stress is adjusted to that indicated by Ogawa (2001) at each temperature (for the quasistatic case $\sigma = g(\epsilon^{\text{p}}, \theta)$ from Eq. (2.20)). Moreover, it is required that $m(\theta)$ match m constant at room temperature; a constant must be added to the functional dependence of m on θ implied by the data in Ogawa (2001). The following empirical relation is thus proposed (where θ is in degrees K)

$$m(\theta) = (1.40 \times 10^{-6})\theta^2 - (8.44 \times 10^{-4})\theta + 0.214, \tag{2.25}$$

as the best fit for the above described experimental data (and therefore most appropriate in the temperature range 77 K $\leqslant \theta \leqslant$ 473 K).

2.4. Strain rate and current density profiles

A proportional straining path is the standard assumption for the calculation of FLD's, i.e. $\epsilon_2 = \rho \epsilon_1$ with ρ a constant such that $-1/2 \leqslant \rho \leqslant 1$. A uniaxial stress state occurs for $\rho = -1/2$ while $\rho = 1$ represents an equibiaxial plane stress state. However, in contrast to the quasistatic forming case of rate-independent solids where the FLD is independent of the strain history $\epsilon_1(t)$, the present calculations on an electromagnetically formed viscoplastic solid need a time-dependent strain profile $\epsilon_1(t)$, in addition to a time-dependent current density profile $j_1(t)$. The strain, strain rate and current density profiles are motivated by the ring calculations of Triantafyllidis and Waldenmyer (2004).

Therefore, since the principal hoop strain rate is shaped as a smooth pulse, a sinusoidal strain rate pulse is assumed for simplicity. Hence for a pulse of duration $4\tau_0$ the principal strains are taken to be

$$\epsilon_1(t) = \frac{\epsilon_{\text{max}}}{2}\left[1 - \cos\left(\frac{\pi t}{4\tau_0}\right)\right], \quad \epsilon_2(t) = \rho \epsilon_1(t), \tag{2.26}$$

which gives for the corresponding strain rate

$$\dot{\epsilon}_1(t) = \frac{\pi \epsilon_{\text{max}}}{8\tau_0} \sin\left(\frac{\pi t}{4\tau_0}\right). \tag{2.27}$$

The maximum principal strain, ϵ_{max}, and the characteristic time, τ_0, are variables of the simulation to be subsequently specified.

The effect of implementing the simplified strain profile above is investigated by comparison with a linear time-dependent strain profile. Again for a pulse duration of $4\tau_0$, the linear strain profile is taken as

$$\epsilon_1(t) = \frac{\epsilon_{\text{max}}}{4\tau_0} t, \quad \epsilon_2(t) = \rho \epsilon_1(t), \tag{2.28}$$

which gives a constant corresponding strain rate

$$\dot{\epsilon}_1(t) = \frac{\epsilon_{\text{max}}}{4\tau_0}. \tag{2.29}$$

Here for comparison purposes ϵ_{max} and τ_0 are equal to those in the sinusoidal strain profile.

Due to the electromagnetic nature of the process, knowledge of the principal current flowing through the sheet is also necessary. Keeping in mind the ring simulations (Triantafyllidis and Waldenmyer, 2004) and the fact that in tube bulging only a current in the hoop direction occurs, with a pulse duration typically half of the strain pulse duration, the following sinusoidal form of the principal current density is adopted for simplicity

$$j_1(t) = J_{\text{max}} \sin\left(\frac{\pi t}{2\tau_0}\right), \quad j_2(t) = 0, \tag{2.30}$$

where J_{max} is the maximum principal current density. It is also assumed that no backward current is allowed to flow, so that for $t > 2\tau_0$, $j_1 = j_2 = 0$. Although the exact nature of the strain and current density time profiles depends on the solution of the coupled electromagnetic and thermomechanical boundary value problem for the relevant experiment, the profiles chosen above are good approximations of the calculated profiles of the

EMF ring work (Triantafyllidis and Waldenmyer, 2004) thus justifying the simplifying assumptions of Eqs. (2.26), (2.27) and (2.30).

To complete these profiles, some physically motivated values for τ_0, $\epsilon_{\max}$ and $J_{\max}$ must be selected. As defined in Eqs. (2.26)–(2.30) τ_0 is one quarter of the total forming time, which equals the time to the electric current's first maximum. This definition is motivated by the work of Triantafyllidis and Waldenmyer (2004), where τ_0 is the time to the first maximum of the electric current in the forming circuit in isolation (without a workpiece). The fully coupled results show a similar time to the electric current's first maximum, and the total forming time is approximately $4\tau_0$. In the present work this characteristic time in combination with $\epsilon_{\max}$ determines the forming rate (see Eq. (2.27)). Without a fully coupled EMF boundary value problem simulation, $\epsilon_{\max}$ must be specified *a priori*. The value of $\epsilon_{\max}$ needs to be greater than the EMF necking strain for all materials and processes of interest, but it should be reasonable as well. If $\epsilon_{\max}$ is chosen high, τ_0 must be large to keep the applied strain rate similar to EMF rates. The method in the present work takes $\epsilon_{\max}$ as a constant (regardless of the strain path ρ), with value $\epsilon_{\max} = 0.8$ which is greater than all of the necking results found here.

With $\epsilon_{\max}$ specified, the strain and strain rate profiles need only τ_0 to be complete. An appropriate value is found by appealing to a property of the viscoplastic material model, namely its overstress ζ. Due to the dynamic nature of an EMF process, the workpiece experiences higher flow stresses than it would in a quasistatic process at identical strains and temperatures. The amount by which the flow stress exceeds the quasistatic flow stress is the overstress, defined as

$$\zeta \equiv \frac{\sigma_{\mathrm{e}}(\sigma_{ij})}{g(\epsilon^{\mathrm{p}}, \theta)} - 1. \tag{2.31}$$

Assuming the material constitutive response is fully defined, ζ can be related to the strain rate through Eq. (2.14). Specifically, assuming a uniaxial process for simplicity and that $\dot{\epsilon}^{\mathrm{p}} = \dot{\epsilon} = \dot{\epsilon}_1$ (a reasonable assumption at the large strains inherent in EMF processes), one has

$$\frac{\dot{\epsilon}_1}{\dot{\epsilon}_0^{\mathrm{p}}} = \left((1 + \zeta)^{1/m(\theta)} - 1\right). \tag{2.32}$$

The maximum strain rate implies

$$\tau_0 = \frac{\pi \epsilon_{\max}}{8 \dot{\epsilon}_0^{\mathrm{p}}} \left((1 + \zeta_{\max})^{1/m(\theta)} - 1\right)^{-1}. \tag{2.33}$$

Thus given an appropriate value of maximum overstress $\zeta_{\max}$, τ_0 is specified; since both m and $\dot{\epsilon}_0^{\mathrm{p}}$ influence the time scale of a process, $\zeta_{\max}$ is chosen to give a physically meaningful forming speed. The value $\zeta_{\max} = 0.15$ is therefore the base case in all subsequent calculations.

Finally, the value for $J_{\max}$ is chosen by considering the temperature increase needed to cause melting. From Eq. (2.8), the temperature increase of the material is due to two sources: plastic work and ohmic heating. As shown in the ring simulations (Triantafyllidis and Waldenmyer, 2004), by the end of the forming process the dissipation of the plastic work and specimen ohmic heating are comparable. This allows the following approximation to Eq. (2.8)

$$\mu c_{\mathrm{p}} \dot{\theta} = 2r(\theta)(j_\alpha j_\alpha). \tag{2.34}$$

From Eq. (2.30) the time-dependent form of the electric current is known, and Eq. (2.34) may be integrated with respect to time if $r(\theta)$ is taken as constant, an assumption that will subsequently be used throughout the simulations. Integrating Eq. (2.34) from $t = 0$ to $t = 4\tau_0$ gives

$$J_{\max} = \left(\frac{\mu c_{\mathrm{p}}(\theta - \theta_0)}{2r\tau_0}\right)^{1/2}. \tag{2.35}$$

If one takes $\theta = \theta_m$, $J_{\max}$ from Eq. (2.35) is such that melting occurs at the end of the simulation, i.e.

$$J_{\mathrm{melt}} = \left(\frac{\mu c_{\mathrm{p}}(\theta_m - \theta_0)}{2r\tau_0}\right)^{1/2}. \tag{2.36}$$

To avoid melting J_{max} must be lower than J_{melt}, and a reasonable value for EMF processes is $J_{max} = 0.15 J_{melt}$. This value, along with $\epsilon_{max} = 0.8$ and τ_0 from Eq. (2.33), completes the base case forming conditions for the present simulations, and the result of the above analysis is $\tau_0 = 78.8$ μs, $J_{max} = 2.69 \ 10^9$ A/m^2 and a maximum forming speed of 3989 s^{-1}.

3. Results and discussion

The goal of the present section is to present an application of the general theory proposed in the previous section. Following the description of the numerical solution algorithm, the section proceeds with the calculation of the FLD for the "base case" alloy and the investigation of its dependence on the various material properties and loading parameters.

3.1. Assumptions and numerical implementation

In the interest of simplicity it is assumed that the material is incompressible. For the large strains encountered during the EMF process, this assumption is quite reasonable since compressibility effects in metals – due to elastic distortion and thermal strain of their crystals – are an insignificant part of the overall plasticity dominated deformation. Consequently, the total strain rate is decomposed into traceless elastic D_{ij}^e ($D_{ii}^e = 0$) and plastic D_{ij}^p ($D_{ii}^p = 0$) parts, the first property requiring a poisson ratio $v = 0.5$ and the second property guaranteed for yield functions which are independent of the first invariant of the stress σ_{ii}.

With these simplifying assumptions in place, the governing equations are cast as a system of first order ODEs. These ODEs are solved using a fourth order Runge–Kutta algorithm. For the solution outside the band only the adiabatic heating Eq. (2.8) and the constitutive equations are required, i.e. one has

$$\dot{x}^A = f_A(x^A, t), \quad x^A \equiv \left[\sigma_1^A, \sigma_2^A, \epsilon_A^p, \theta^A\right], \tag{3.1}$$

where σ_1^A and σ_2^A are Cauchy principal stresses. Inside the localized band, the four continuity Eqs. (2.1), (2.2), (2.4) and (2.6) give six scalar equations, which in addition to energy balance Eq. (2.8) and the four constitutive equations detailed in Section 2.2 (three for the in-plane stresses $\sigma_{\alpha\beta}$ and one for the internal variable ϵ^p) can completely determine the eleven variable electromechanical state inside the band ($F_{\alpha\beta}$ (4), $\sigma_{\alpha\beta}$ (3), j_α (2), ϵ^p (1), θ (1)) in terms of the known counterpart field quantities outside the band. Note, the j_i^B are obtained directly (without recourse to ODEs) from Eqs. (2.4)–(2.7), while due to the incremental nature of plasticity calculations, the rate forms of Eqs. (2.1) and (2.2) are required. Once again, the resulting equations are cast as a system of first order ODEs

$$\dot{x}^B = f_B(x^B, t), \quad x^B \equiv \left[\sigma_{11}^B, \sigma_{12}^B, \sigma_{22}^B, F_{11}^B, F_{21}^B, F_{12}^B, F_{22}^B, \epsilon_B^p, \theta^B\right], \tag{3.2}$$

where the t-dependent terms in $f_B(x^B, t)$ are functions of x^A.

The numerical localization calculations require establishing a necking criterion. Localization occurs when ϵ_B^p becomes unbounded for a finite value of ϵ_A^p, which is numerically implemented as when $\dot{\epsilon}_B^p / \dot{\epsilon}_A^p > 10$. The value 10 is chosen arbitrarily but is adequately large to have a negligible effect on the calculated necking strain. The necking of the imperfect sheet depends on the angle Φ of the imperfection in the reference configuration (see Fig. 2), which can take any value $0 \leqslant \Phi < \pi/2$. The value that minimizes the necking strain outside the band gives the sought forming limit strains. One must therefore test through the entire $[0, \pi/2)$ range of band angles (satisfactory accuracy is obtained using increments of $\pi/180$) for each load path ρ, and this results in $\Phi = 0$ for $0 \leqslant \rho \leqslant 1$ but $\Phi \neq 0$ for $-1/2 \leqslant \rho < 0$. The advantage of the full Lagrangian description used is best appreciated at this point, since the band rotation during deformation is automatically taken care of by the large strain kinematics (the band angle Φ is kept constant). Alternative formulations using current configuration would have required a more complicated kinematic description (to account for the changing band orientation ϕ), an approach that can easily lead to errors.

Finally, numerical precision of the localization strain calculations must be checked. First, the quasistatic case has an analytical solution for $\rho = 0$ and $\beta = 2$ (isotropic J_2 flow theory of plasticity) of ϵ_{neck} obtained at the maximum of the nominal stress. Using $\xi = 0.001$ and an adequately small time step (see below) the

analytical solution is recovered. Second, for both the quasistatic and rate-dependent cases the time step, Δt, is chosen by requiring less than 0.001 change in necking strain for any Δt decrease. This results in the nondimensional time steps $\Delta t/\tau_0 \approx 3 \times 10^{-7}$ for the quasistatic process and $\Delta t/\tau_0 \approx 2 \times 10^{-5}$ for the EMF processes.

3.2. Forming limit diagrams

The numerically calculated FLD's are presented in Figs. 3–12. More specifically, the influence of material properties is presented in Figs. 3–8, while the influence of various loading parameters is given in Figs. 9–12.

The effect of EMF on the FLD is presented in Fig. 3, with six forming limit curves, three each for EMF and quasistatic forming conditions (quasistatic results are obtained from the dynamic simulation by imposing a low forming speed, minimal strain-rate sensitivity and an isothermal process). For each one of the three yield surfaces presented in Section 2.2.1 there are two FLD curves, one for an EMF process and one for its quasistatic counterpart. Use of an EMF process results in a significant increase in forming limit strains as compared to a quasistatic one of the same ρ, and the increase is dependent on the yield surface. This dependence is important in the $\rho > 0$ region, while $\rho \leqslant 0$ shows negligible influence of the yield surface choice. Notice that the necking strains for the isotropic $\beta = 2$ surface (von Mises) are unrealistic even for the quasistatic loading. The reason is the low curvature of the yield surface, in particular near $\rho = 1$, a known deficiency of flow theory models (see discussion in Stören and Rice, 1975). Of the three yield surface models considered here, the anisotropic nonquadratic surface, Yld94, is the best choice based on comparison with the experimental quasistatic FLD presented in LeRoy and Embury (1978). Hence in all subsequent calculations the Yld94 model is used. From the curves generated with this yield surface, the EMF process provides between a 25% ($\rho = 1$) and 225% ($\rho = -1/2$) increase in forming limits over a quasistatic process.

The necking angle ϕ_{neck} of the weak band (where ϕ is the angle of the band in the current configuration related to its reference configuration counterpart Φ by $\tan(\phi) = \tan(\Phi)\exp(\epsilon_1 - \epsilon_2)$) is plotted for the base case EMF process against the strain ratio $\rho = \epsilon_2/\epsilon_1$ in Fig. 4a. For $\rho \geqslant 0$, $\phi_{neck} = 0$, while for $\rho < 0$, $\phi_{neck} \neq 0$; ϕ_{neck} approaches 40° as $\rho \to -1/2$. These values of ϕ for both $\rho < 0$ and $\rho \geqslant 0$ mirror known quasistatic results (see Stören and Rice, 1975; Hill, 1952), indicating that ϕ_{neck} is insensitive to EMF processes.

In order to give an idea of a typical temperature increase due to the application of an EMF process the temperatures at the onset of necking for the base case EMF process, both outside (θ^A) and inside (θ^B) the weak band, are shown in Fig. 4b plotted against the strain ratio $\rho = \epsilon_2/\epsilon_1$. A temperature rise between 30 and 80 K in the sheet (A) is predicted, with the minimum at $\rho = 0$ and the maximum at $\rho = 1$. Moreover, there is a significant temperature difference between the sheet (A) and weak band (B) due to higher plastic strain rate and higher current density. The ramifications of this additional rise in temperature inside the band will be discussed subsequently.
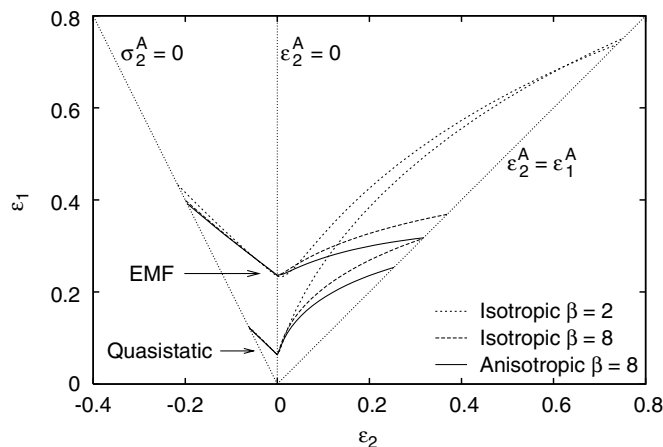

Fig. 3. Comparison of EMF versus quasistatic forming limit curves for an alloy with a given uniaxial response for three different yield surfaces.
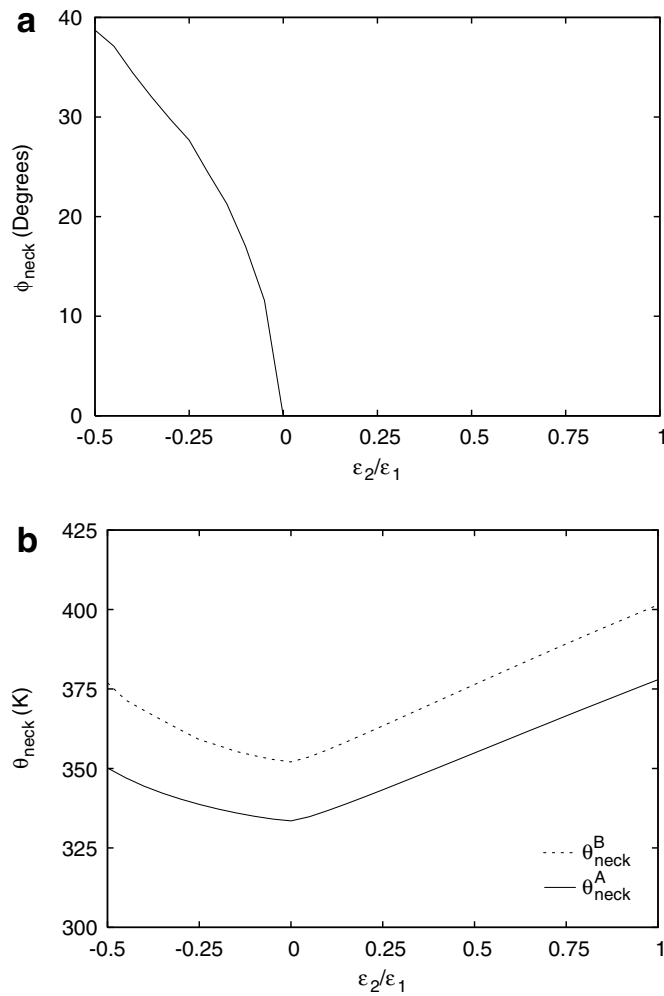
Fig. 4. (a) Angle of the weak band in the current configuration at the onset of necking ϕ_{neck} versus principal strain ratio ρ for the base case EMF process. (b) Temperature at the onset of necking θ_{neck} as a function of the principal strain ratio ρ both outside (A) and inside (B) the weak band for the base case EMF process.

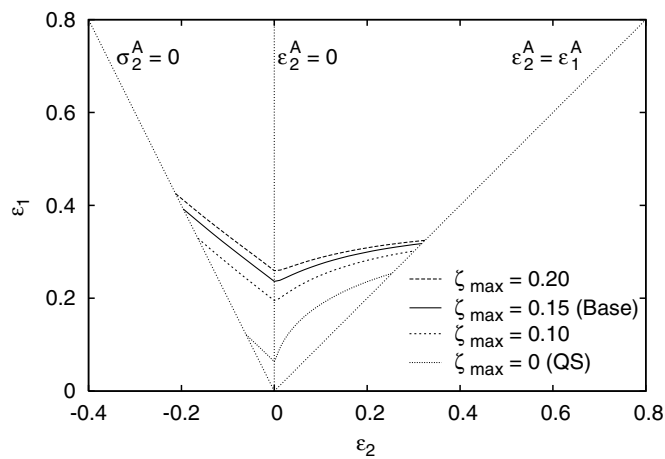Fig. 5. Influence of the process's characteristic time τ_0 (based on the resulting maximum overstress ζ_{max}) on the forming limit curve.

Fig. 5 shows the influence on necking of the speed of the EMF process, with the quasistatic (QS) forming limits shown for comparison. Changing the loading speed is equivalent to changing the nondimensional time scale $\dot{\epsilon}_0^p \tau_0$, which for consistency (since m also controls viscosity) is driven by the maximum overstress ζ_{max} as
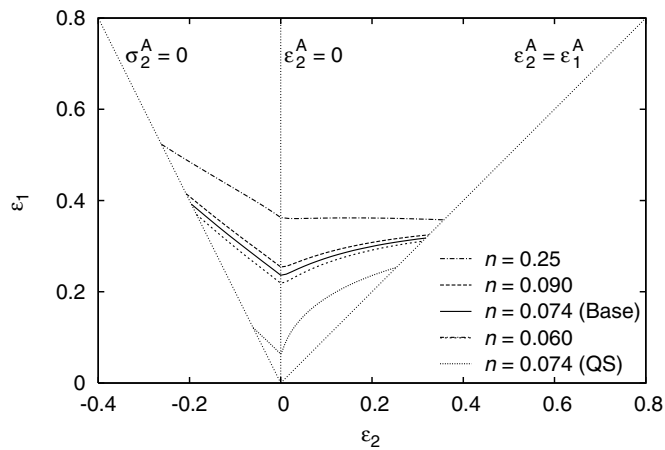
Fig. 6. Influence of the hardening exponent n on the forming limit curve.

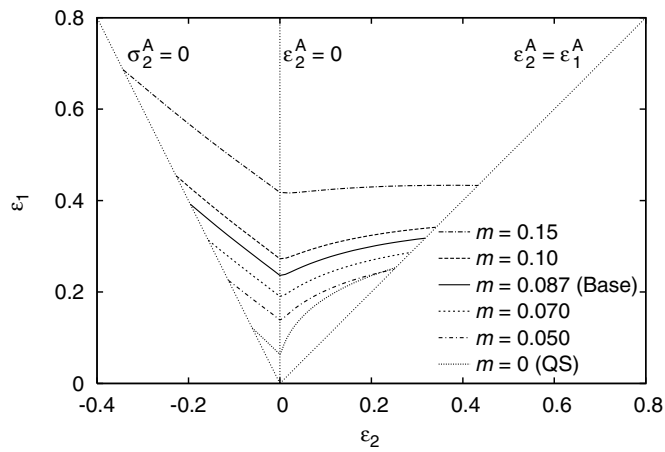Fig. 7. Influence of the rate sensitivity exponent m (with nondimensional time scale $\dot{\epsilon}_0^p \tau_0$ kept constant) on the forming limit curve.
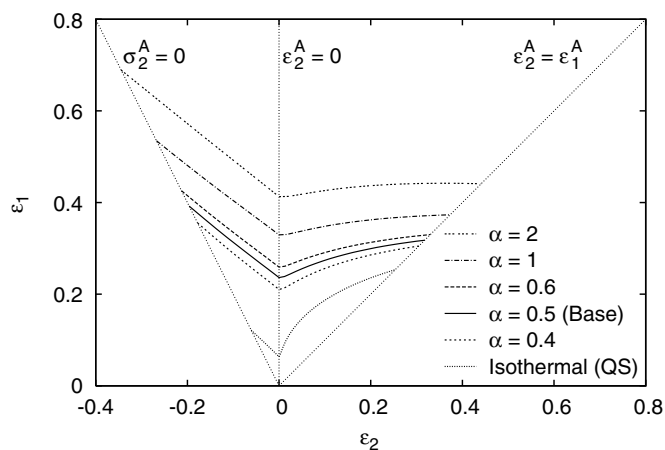

Fig. 8. Influence of the temperature sensitivity exponent α on the forming limit curve.

discussed in Section 2.4. Increasing ζ_{max} corresponds to increasing the forming speed, which results in higher necking strains as expected from the material's viscosity. The increase in ductility due to EMF effect is greatest for $\rho < 0$, where the forming limit curve shifts up, and decreases with increasing ρ.
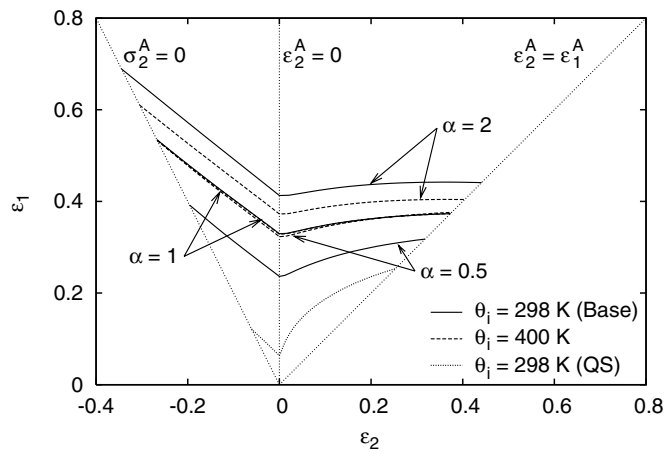
Fig. 9. Influence of initial temperature θ_i on the forming limit curve for three different thermal sensitivity exponents.
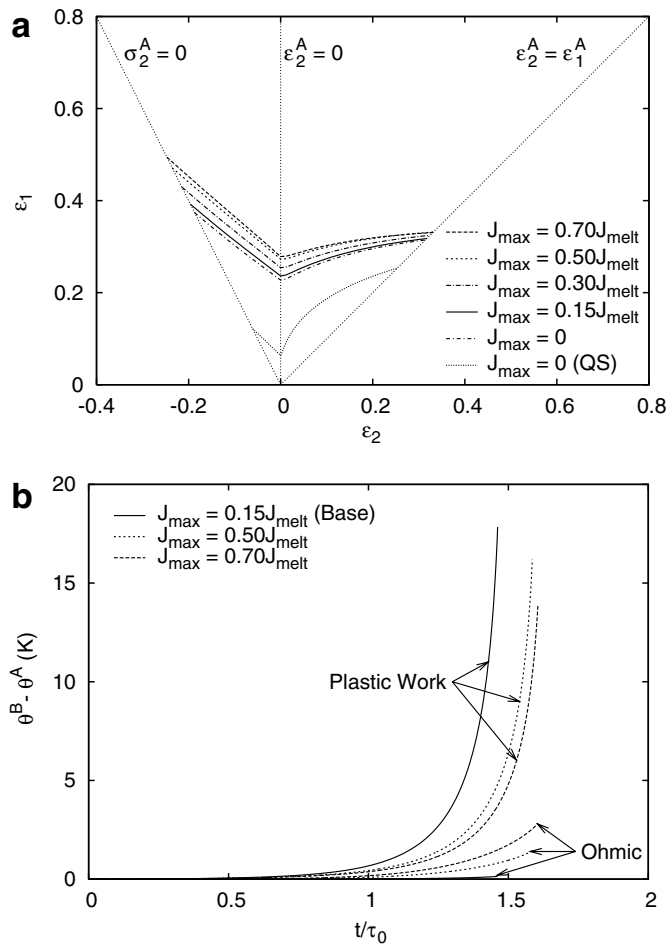
Fig. 10. (a) Influence of electric current density J_{max} on the forming limit curves for constant rate sensitivity exponent m. (b) Influence of electric current density J_{max} on the temperature difference between weak band (B) and sheet (A) for constant rate sensitivity exponent m. The temperature differences due to ohmic heating and plastic work are calculated separately.

The influence of the hardening exponent n is shown in Fig. 6. An increase in n is known to increase the forming limits for a quasistatic process (e.g. Stören and Rice, 1975), and the same influence is seen here for an EMF process. The increase in necking strains is found for both $\rho < 0$ and $\rho \geqslant 0$, with the minimum increase occurring at $\rho = 1$. Moreover with the values of n considered here $0 \leqslant n \leqslant 0.25$, there is a parallel shift
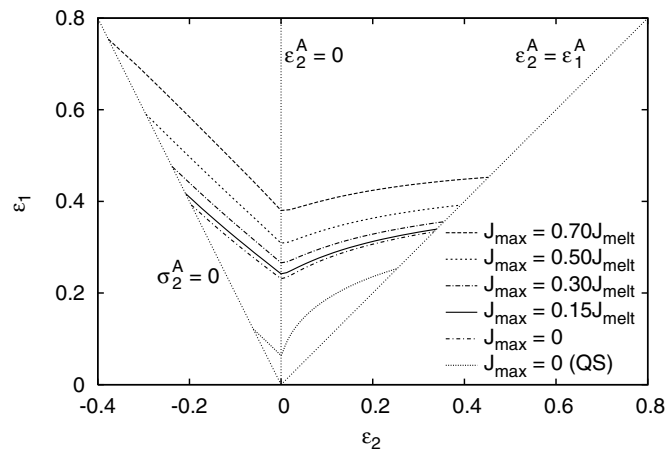
Fig. 11. Influence of electric current density J_{max} on the forming limit curves for a temperature-dependent strain-rate sensitivity $m(\theta)$.
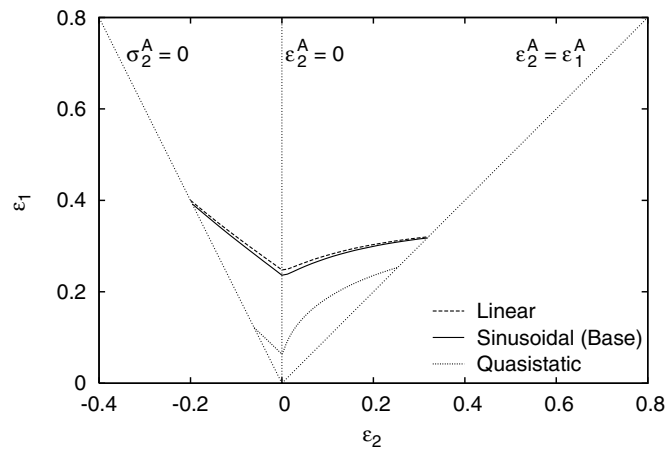

Fig. 12. Influence of the assumed strain profile on the forming limit curve.

in the forming limit curves for $\rho < 0$. For $\rho > 0$ with small values of n the necking strains increase with increasing ρ while for large values of n this trend is reversed, with ϵ_{neck} decreasing for increasing ρ.

Fig. 7 shows the influence on ductility of the strain-rate sensitivity exponent m. As expected from the thermally insensitive case (see Hutchinson and Neale, 1977), the forming limits increase with increasing m, with the minimum ductility increase occurring at $\rho = 1$. Here the influence of m is calculated for a fixed maximum strain rate (i.e. $\dot{\epsilon}_0^p \tau_0$ fixed), which implies that the pulse time for all experiments remains fixed.

The effect of the temperature sensitivity exponent α is presented in Fig. 8. Recall that for temperature sensitive solids an increase in temperature reduces the flow stress, i.e. weakens the material. From Eqs. (2.14) and (2.20) it also follows that a lower α indicates stronger temperature sensitivity. Since the weak band receives more heating than the sheet (see Fig. 4b) through additional plastic work and higher current densities, consequently an increased temperature sensitivity weakens the band more in relation to the sheet, which encourages necking. This mechanism explains why a decrease in α (i.e an increase in temperature sensitivity) causes a decrease in the forming limits for all values of ρ.

In Fig. 9 is shown the influence of the initial temperature θ_i on the FLD. The sheet and weak band in all cases have the same initial temperature; the base case initial temperature is the reference temperature $\theta_0 = 298$ K. The form of the uniaxial response, Eqs. (2.14) and (2.20), indicates that an increase in temperature makes the flow stress, for subsequent temperature changes, less temperature sensitive for $\alpha < 1$, equally temperature sensitive for $\alpha = 1$ and more temperature sensitive for $\alpha > 1$. Also, Fig. 8 indicates that the forming limits increase with decreasing temperature sensitivity. These observations explain the influence of θ_i on the forming limits. In particular, $\alpha = 1$ shows negligible dependence on θ_i, while calculations with thermal

sensitivity values $\alpha = 0.5$ and 2 indicate that for increasing θ_i forming limits for $\alpha < 1$ increase and forming limits for $\alpha > 1$ decrease.

Fig. 10a presents the influence of the electric current density on the FLD. Plastic dissipation produces two orders of magnitude more temperature difference between weak band and sheet than ohmic dissipation in the base case EMF process. This indicates the electric current primarily heats the workpiece uniformly (i.e. the same amount inside and outside the band), and by the results in Fig. 9 one expects increased forming limits with increased electric current. However, as J_{max} approaches J_{melt} the temperature difference (between weak band and sheet) due to ohmic dissipation approaches that of plastic dissipation. For large J_{max} ohmic dissipation has a strong negative influence on the forming limits since an increased temperature difference encourages necking. The result is the upper bound on the forming limits for increasing J_{max} observed in Fig. 10a.

In Fig. 10b the temperature difference between weak band and sheet $\theta^B - \theta^A$, for the cases $J_{max} = 0.15 J_{melt}$, $J_{max} = 0.50 J_{melt}$ and $J_{max} = 0.70 J_{melt}$, is plotted with respect to nondimensional time t/τ_0 for the strain path $\rho = 0$. To illustrate the mechanism behind the upper bound on the forming limits for increasing J_{max}, the temperature difference is divided into a part due to plastic dissipation and a part due to ohmic dissipation. As J_{max} increases the plastic dissipation difference between zones A and B is reduced while the corresponding difference in ohmic dissipation dramatically increases due to thinning of the weak band and the subsequent electric current density increase. Between $J_{max} = 0.50 J_{melt}$ and $J_{max} = 0.70 J_{melt}$ these two influences add to produce minimal change in $\theta^B - \theta^A$; this correlates with negligible change in the forming limits (see Fig. 10a). The increased $\theta^B - \theta^A$ due to unequal ohmic heating encourages necking and counteracts the uniform temperature increase that delays necking (see Fig. 9).

Fig. 11 shows the results of implementing a temperature-dependent strain-rate sensitivity $m(\theta)$ as described by Eq. (2.25). Since the strain-rate sensitivity increases with temperature, its effect overrides the influence of the ohmic dissipation. The forming limits thus behave monotonically with respect to the electric current. This indicates the temperature dependence of the strain-rate sensitivity strongly influences the FLD for EMF processes.

The influence of the strain profile on necking is presented in Fig. 12. The sinusoidal base case profile (Eqs. (2.26) and (2.27)) is compared with the simple linear profile (Eqs. (2.28) and (2.29)), where ϵ_{max} and τ_0 are kept at the base case values for both profiles. Fig. 12 shows the profile has little influence on the forming limits, and this further supports the use of Eqs. (2.26) and (2.27) as a reasonable approximation to the actual strain profile encountered during an EMF process.

Figs. 3–12 illustrate how the electromagnetic forming process enhances sheet ductility. The effects of material properties and EMF process characteristics have been examined in detail. The following section gives a concise summary of the above results and a discussion of potential future work.

4. Conclusion

An advantage that electromagnetic forming (EMF) has over conventional forming techniques is an increase in ductility for some metal alloys of industrial interest. In the prediction of ductility limits for conventional forming techniques the forming limit diagram (FLD) is a useful design tool, and thus in the present work, the classical free-expansion FLD concept for flat sheets is extended to include electromagnetic forming operations. In particular, a flat sheet of strain hardening, strain-rate sensitive and temperature sensitive material which is subjected to in-plane electric currents and a high strain rate biaxial loading is modeled using a Marciniak–Kuczynski type weak band analysis. The imposed forming conditions are chosen to correspond with those of actual axisymmetric EMF processes. Though the solution of a fully coupled EMF boundary value problem is required to exactly model the behavior of the metal workpiece under EMF conditions, the present FLD analysis provides significant insight into the formability of the aluminum sheet for EMF processes by focusing on conditions for the onset of a localized necking.

The present analysis shows a significant increase in ductility from quasistatic to EMF conditions; the greatest difference occurs for strain paths with load path strain ratio $\rho \leqslant 0$. In the case $\rho < 0$ the angle of the weak band at necking in the reference configuration $\Phi_{neck} \neq 0$, and, when compared to results for $\rho > 0$, the predicted forming limits for $\rho \leqslant 0$ are insensitive to imperfection amplitude ξ and the yield surface choice. The reason for this ductility increase is the high strain rates, compared to conventional

forming, inherent in an EMF process, given that the strain-rate sensitivity of the material delays the onset of necking (see Hutchinson and Neale, 1977). The present work shows that the details of the strain time profile do not significantly affect the forming limits, though the strain rate of the loading does. Increasing the electric current density can also increase ductility, though above a certain current density no additional ductility increase is found. However, the influence of the initial temperature θ_i depends on the temperature sensitivity exponent α, which indicates that the influence of electric current density will also vary with the material properties. Moreover, if a temperature-dependent strain-rate sensitivity $m(\theta)$ is implemented, such that m increases with temperature in accordance to existing experimental data, the limit on the ductility increase for increasing current density disappears and strains at the onset of necking for a fixed ρ increase monotonically with increasing current density.

The material constitutive response is of paramount importance in determining forming limits for EMF processes. The anisotropy and yield surface details strongly influence the forming limits in the $\rho > 0$ region, while $\rho \leqslant 0$ is largely unaffected by these aspects. However, the EMF formability is affected for all values of ρ by the hardening exponent n; ductility increases as n increases. Similarly, increasing the strain-rate sensitivity exponent m for a fixed forming speed increases the onset of necking strains. The temperature sensitivity exponent α also has the same correlation with ductility. Increasing α increases forming limits.

In addition to the influences on formability investigated in the present work, there are a number of other possible factors to be addressed. It is important to recall that all the results here depend on the imperfection parameter ξ, most significantly for strain paths with $\rho > 0$, a rather undesirable – but inevitable under adopted simplifying assumptions – feature of the FLD analysis. There is also some controversy about the magnitude and/or existence of a free forming EMF ductility increase over conventional techniques (see, for example, Oliveira and Worswick, 2003; Zhang and Ravi-Chandar, 2006; Oliveira et al., 2005). This issue should be investigated in the light of complete experimental evidence, especially since the material constitutive response is alloy-dependent (e.g. the transition strain rate varies widely between aluminum alloys (Tirupataiah and Sundararajan, 1994)). Moreover, inertia has been shown to be a factor in high strain rate formability (e.g. Hu and Daehn, 1996; Mercier and Molinari, 2004), and contact effects are known to strongly influence high velocity forming (e.g. Balanethiram and Daehn, 1994; Imbert et al., 2005). Finally, the present work makes the implicit assumption that the thermal response of the material is the same under quasistatic and EMF forming speeds. At the time scale of EMF forming (i.e. on the order of 50 μs) the material thermal constitutive response may vary greatly from that observed at conventional speeds. Further experimental evidence is needed to characterize the material's response to temperature changes over these time scales. However, in spite of the adopted simplifying assumptions and given the independence of results of strain profile, we believe that the current investigation can provide a useful and fairly accurate predictive tool for making ductility calculations for EMF processes.

Acknowledgments

Appendix A. Justification of necking criterion

The necking criterion used in the electromagnetic FLD calculations is a weak band initial imperfection criterion, similar in spirit to the thickness inhomogeneity criterion first introduced by Marciniak and Kuczynski (1967) to account for necking in the biaxial stretching region of an elastoplastic solid within the framework of classical plasticity theory (smooth yield surface and normality). The dependence of the necking strain predictions on the size of the initial imperfection is a rather undesirable feature of this approach, which has lead to the proposition of alternative necking criteria. For the case of rate-independent solids, Stören and Rice (1975) proposed a necking criterion based on the loss of ellipticity in the equations governing the incremental plane stress deformation of the sheet, which are based on a deformation

type theory of plasticity, thus predicting necking independently of imperfections. Unfortunately, this approach cannot be generalized for viscoplastic solids, whose incremental response is governed by their elastic moduli.

To avoid the assumption of an initial imperfection, Triantafyllidis et al. (1997) proposed a linearized perturbation criterion for the stability of elastoviscoplastic solids, which was based on the growth/decay of the perturbation acceleration in response to a velocity perturbation of unit norm. This criterion was expanded upon by Massin et al. (1999) and generalized for continua by Nestorović et al. (2000). Unlike the compressive load cases for which it was conceived, the application of this linearized perturbation criterion to the analysis of necking under tension gives unrealistic results (critical strain decreases for increasing load rates) and hence had to be abandoned as a candidate necking criterion. However, the comparison of the necking predictions for the linearized perturbation and initial imperfection criteria for the case of an elastoviscoplastic bar subjected to uniaxial tension is both novel (to the best of the authors' knowledge) and useful and merits a brief presentation.

A.1. Kinematic and constitutive relations

For simplicity, no thermal effects are considered and the material in the uniaxially loaded bar is treated as incompressible. The latter assumption yields

$$al = AL, \tag{A.1}$$

where a (A) is the current (reference) cross-section area and l (L) is the current (reference) length. In this finite strain problem the strain, ϵ, is defined as

$$\epsilon \equiv \ln(l/L), \tag{A.2}$$

and the first Piola–Kirchhoff stress, Π (force/reference area), can be expressed with the help of Eqs. (A.1) and (A.2) in terms of the Cauchy stress, σ, and strain, ϵ, by

$$\Pi = \sigma \exp(-\epsilon). \tag{A.3}$$

The uniaxial strain is decomposed into elastic, ϵ^e, and plastic, ϵ^p, parts, and the constitutive response reads

$$\sigma = E\epsilon^e, \quad \epsilon^e = \epsilon - \epsilon^p. \tag{A.4}$$

For a viscoplastic material the relation between $\dot{\epsilon}^p$ and the solid's quasistatic uniaxial response $g(\epsilon^p)$ is governed by the function F,

$$\dot{\epsilon}^p = F(\sigma, g(\epsilon^p)). \tag{A.5}$$

Here two versions of the function F, namely F_p and F_l, will be used. F_p is the same power law constitutive model that was used for the FLD calculations, i.e.

$$F_p = \dot{\epsilon}_0^p \left[\left(\frac{\sigma}{g(\epsilon^p)} \right)^{1/m} - 1 \right], \tag{A.6}$$

where m is the strain-rate sensitivity exponent and $\dot{\epsilon}_0^p$ is the viscoplastic time scale. F_l represents an alternative linear overstress model

$$F_l = \frac{\dot{\epsilon}_0^p}{\sigma_y} [\sigma - g(\epsilon^p)], \tag{A.7}$$

where σ_y is the material's uniaxial yield stress. It is important to note that $\dot{\epsilon}_0^p$ is not equivalent between the two constitutive laws. The uniaxial quasistatic response for both versions of F is

$$g(\epsilon^p) = \sigma_y \left[1 + \frac{\epsilon^p}{\epsilon_y} \right]^n, \tag{A.8}$$

where $\epsilon_y = \sigma_y/E$ and n is the hardening exponent. Base case values of material parameters from the FLD simulations (see Tables 1 and 2) are also used here.

A.2. Linearized perturbation analysis

For the one-dimensional bar model, the linearized perturbation stability criterion, introduced in Trian-tafyllidis et al. (1997), works as follows: consider that at time t_0 a perturbation in the field quantities of zone B of the bar (see insert in Fig. A.1) is introduced and let $\Delta f \equiv f_B - f_A$ denote the difference in the field quantity f between the perturbed (B) and unperturbed (A) parts of the bar. Furthermore assume that the perturbation results in a given $\Delta\dot{\epsilon} > 0$. In this linearized stability analysis a perturbation is defined to be stable when the resulting $\Delta\ddot{\epsilon} < 0$, i.e. when the rate of $\Delta\dot{\epsilon}$ decreases near time t_0. One can thus define $\Lambda \equiv \Delta\ddot{\epsilon}/\Delta\dot{\epsilon}$; an unstable bar results in $\Lambda > 0$. Hence, $\Lambda = 0$ signals the onset of a necking instability, and the corresponding critical condition is independent of the size of the perturbation.

Equilibrium of the bar implies

$$\Delta\Pi = 0. \tag{A.9}$$

Linearizing about the principal solution (zone A) the response of the bar to a perturbation in $\dot{\epsilon}$, one obtains from the first and second rate of Eq. (A.9)

$$\Delta\dot{\Pi} = \mathcal{S}_{11}\Delta\dot{\epsilon} + \mathcal{S}_{10}\Delta\epsilon = 0 \tag{A.10}$$

and

$$\Delta\ddot{\Pi} = (\mathcal{S}_{22}\Lambda + \mathcal{S}_{21})\Delta\dot{\epsilon} + \mathcal{S}_{20}\Delta\epsilon = 0, \tag{A.11}$$

where the coefficients $\mathcal{S}_{10}$, $\mathcal{S}_{11}$, $\mathcal{S}_{20}$, $\mathcal{S}_{21}$ and $\mathcal{S}_{22}$ are given by

$$
\begin{aligned}
\mathcal{S}_{10} &= -\left[(E-\sigma)\dot{\epsilon} + \dot{\sigma} + E^2\frac{\partial F}{\partial\sigma}\right], \\
\mathcal{S}_{11} &= E - \sigma, \\
\mathcal{S}_{20} &= E^2\frac{\partial F}{\partial\sigma}\left(E\frac{\partial\dot{F}}{\partial\dot{\sigma}} - \frac{\partial\dot{F}}{\partial\dot{g}}\frac{\partial\dot{g}}{\partial\dot{\epsilon}^{\mathrm{p}}} + 2\dot{\epsilon}\right) \\
&\quad - E^2\frac{\partial\dot{F}}{\partial\sigma} + E(\dot{\epsilon}^2 - \ddot{\epsilon}) - (\ddot{\sigma} - 2\dot{\sigma}\dot{\epsilon} + \sigma\dot{\epsilon}^2 - \sigma\ddot{\epsilon}), \\
\mathcal{S}_{21} &= -\left[2(E-\sigma)\dot{\epsilon} + 2\dot{\sigma} + E^2\frac{\partial\dot{F}}{\partial\dot{\sigma}}\right], \\
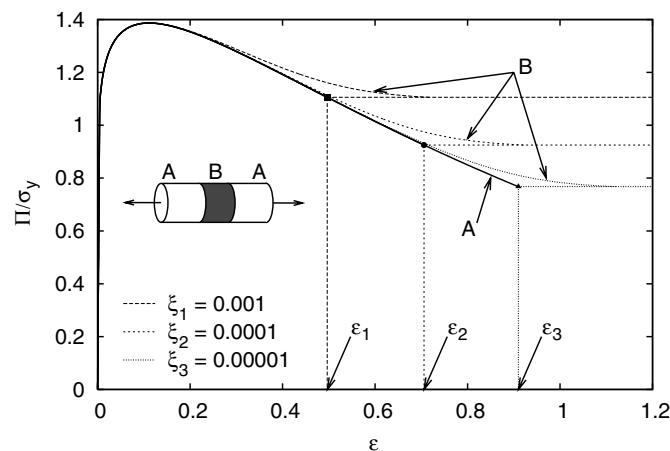\mathcal{S}_{22} &= E - \sigma.
\end{aligned}
\tag{A.12}
$$

Fig. A.1. Nondimensional first Piola–Kirchhoff stress (Π/σ_y) versus logarithmic strain for three values of imperfection parameter ξ based on the power law constitutive model and the sinusoidal strain profile. The force versus strain is plotted both outside (A) and inside (B) the weak band thus illustrating the existence of the necking strain.

Writing Eqs. (A.10) and (A.11) in matrix form gives

$$\begin{bmatrix} \mathcal{S}_{11} & \mathcal{S}_{10} \\ \mathcal{S}_{22}\varLambda + \mathcal{S}_{21} & \mathcal{S}_{20} \end{bmatrix} \begin{pmatrix} \Delta\dot{\epsilon} \\ \Delta\epsilon \end{pmatrix} = 0. \tag{A.13}$$

Nonzero solutions to the above matrix equation exist only if the determinate of the coefficient matrix is zero, which implies

$$\varLambda = \frac{\mathcal{S}_{11}\mathcal{S}_{20} - \mathcal{S}_{10}\mathcal{S}_{21}}{\mathcal{S}_{10}\mathcal{S}_{22}}. \tag{A.14}$$

Notice that $\varLambda$ is a function of the time-dependent solution of the viscoplastic bar problem, and for a well posed problem at the onset of the bar's loading $\varLambda < 0$. An instability occurs when $\varLambda = 0$, which from Eq. (A.14) gives the following condition at the onset of instability

$$\mathcal{S}_{11}\mathcal{S}_{20} - \mathcal{S}_{10}\mathcal{S}_{21} = 0. \tag{A.15}$$

To implement this criterion the principal solution of the elastoviscoplastic bar is formulated as a set of two first order ODEs from the rate of Eq. (A.4)$_1$ and Eq. (A.5), namely

$$\dot{\mathbf{x}} = f(\mathbf{x}, t), \quad \mathbf{x} \equiv [\sigma, \epsilon^{\mathrm{p}}]. \tag{A.16}$$

These are solved with a fourth order Runge–Kutta algorithm, and numerical precision is ensured by keeping the same time step as used in the FLD calculations. The necking criterion, $\varLambda = 0$, is detected via a simple bisection method.

A.3. Initial imperfection analysis

The analysis here is the one-dimensional (uniaxial stress) version of the two-dimensional theory presented in Section 2. As a strain profile is applied to the bar, the strains outside, ϵ^A, and inside, ϵ^B, the weak band are compared (see the inset diagram in Fig. A.1). Necking occurs when the ratio of the plastic strain rate inside the band to that outside the band becomes unbounded, i.e. when $\dot{\epsilon}_B^{\mathrm{p}}/\dot{\epsilon}_A^{\mathrm{p}} \to \infty$. The imperfection is implemented as $\sigma_y^B = (1 - \xi)\sigma_y^A$, with the reference imperfection parameter $\xi = 0.001$ carried over from the FLD calculations.

From the rate of force continuity across the band, i.e. continuity of the first Piola-Kirchhoff stress rate $\dot{\varPi}$, one obtains with the help of Eq. (A.3) the following relation between the stress and strain rates inside and outside the weak band

$$\exp(-\epsilon^A)(\dot{\sigma}^A - \dot{\epsilon}^A\sigma^A) = \exp(-\epsilon^B)(\dot{\sigma}^B - \dot{\epsilon}^B\sigma^B). \tag{A.17}$$

This equation along with the Eqs. (A.4)$_1$ and (A.5) determine the solution in the weak band. As in the linearized perturbation analysis, the principal solution (outside the band) is formulated from the rate of Eq. (A.4)$_1$ and Eq. (A.5) as two ODEs. Then, these two equations (the rate of Eq. (A.4)$_1$ and Eq. (A.5)) applied inside the band and Eq. (A.17) give three ODEs for the three unknowns σ^B, ϵ^B and ϵ_B^{p}, i.e.

$$\dot{\mathbf{x}}^B = f(\mathbf{x}^B, t), \quad \mathbf{x}^B \equiv [\sigma^B, \epsilon^B, \epsilon_B^{\mathrm{p}}], \tag{A.18}$$

where the t-dependent terms are functions of the principal solution $\mathbf{x}^A(t)$. These ODEs are solved with a fourth order Runge–Kutta algorithm using the same time steps as the FLD calculations. The necking criterion is numerically implemented as when $\dot{\epsilon}_B^{\mathrm{p}}/\dot{\epsilon}_A^{\mathrm{p}} > 10$. This value, 10, is chosen in accordance with the previous FLD calculations and has negligible effect on the computed critical strains.

A.4. Strain profile selection

The applied strain profile must be specified for the completion of the simulation. Two different profiles are considered, a sinusoidal profile and a linear profile that match the ϵ_1 profiles taken in the FLD calculations, which are given by

$$\epsilon(t) = \frac{\epsilon_{\max}}{2} \left[1 - \cos\left(\frac{\pi t}{4\tau_0} \right) \right], \quad \epsilon(t) = \epsilon_{\max} \frac{t}{4\tau_0}. \tag{A.19}$$

Due to the same considerations as in the FLD work, $\epsilon_{\max} = 1$ is used in the present work, and τ_0 is varied through the term $\dot{\epsilon}_0^{\mathrm{p}} \tau_0$, with further discussion following in Section A.5.

A.5. Results and discussion

The section compares the onset of necking predictions from the above introduced two criteria and for the four combinations of two constitutive laws, power law F_{p} and linear overstress F_{l}, and two load profiles, sinusoidal and linear.

Fig. A.1 presents the dimensionless first Piola-Kirchhoff stress, Π, versus logarithmic strain, ϵ, in the bar with power law viscosity subjected to a sinusoidal strain profile. The initial imperfection model is examined, and Π/σ_y versus ϵ is given for both outside (A) and inside (B) the band. The rate of deformation is set by the dimensionless measure of characteristic speed $(\dot{\epsilon}_0^{\mathrm{p}} \tau_0)^{-1}$, with $(\dot{\epsilon}_0^{\mathrm{p}} \tau_0)^{-1} = 26.9$. Results for three different values of the imperfection parameter ξ are calculated.

In a quasistatic process necking is predicted at the maximum force (equivalently maximum Π). For a viscoplastic bar the maximum force during a process depends on the loading rate due to its strain-rate sensitivity. From equilibrium the force in the bar outside and inside the weak band must be equal, but due to the relative weakness of the band $\dot{\epsilon}_B^{\mathrm{p}} > \dot{\epsilon}_A^{\mathrm{p}}$. This unequal strain rate allows the weak band to reach higher stresses than the outside zone thus permitting considerable elongation past the point where the maximum force occurs; the strain-rate sensitivity stabilizes the weak band by strengthening the material as the strain rate increases. Necking occurs when for some force Π/σ_y the strain rate inside the band tends to infinity. The imperfection parameter strongly affects the force level at which this necking phenomenon happens.

The dimensionless first Piola–Kirchhoff stress versus strain response of the power law elastoviscoplastic bar subjected to a sinusoidal strain profile and for characteristic speeds $(\dot{\epsilon}_0^{\mathrm{p}} \tau_0)^{-1}$ from 0.159 to 100 is presented in Fig. A.2. Necking calculations for the initial imperfection analysis with three different imperfections ($\xi = 10^{-3}$, 10^{-4}, 10^{-5}) and the linearized perturbation method are shown. The initial imperfection calculations, for each fixed ξ value, show higher necking strains for higher speeds. The linearized perturbation criterion shows the opposite trend, agreeing with the initial imperfection model's necking strain prediction at quasistatic speeds (maximum force) and predicting decreasing necking strains from there as the speed increases. Also, as ξ decreases the initial imperfection criterion necking strain prediction increases as noted previously, and for
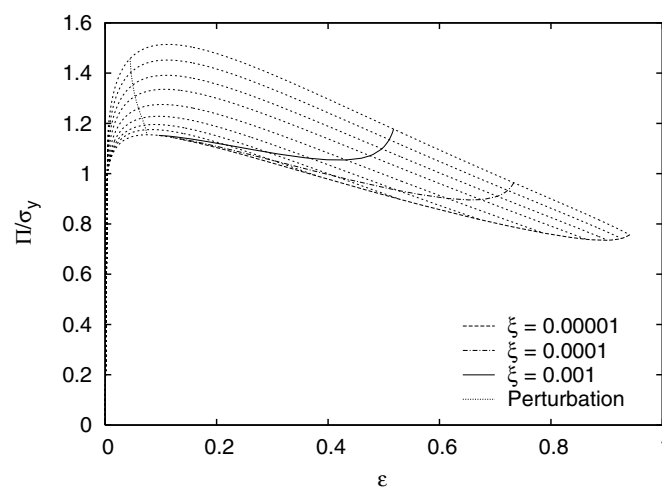

Fig. A.2. The nondimensional first Piola–Kirchhoff stress versus logarithmic strain for varying loading rates (the stress increases with increasing loading rate), based on the power law constitutive model and the sinusoidal strain profile. The onset of necking strain prediction from the linearized perturbation criterion is recorded, as is the necking prediction from the initial imperfection analysis for three values of imperfection parameter ξ.

all ξ values an upper limit on the necking strain exists such that above a certain speed further loading rate increases have little influence.

In Fig. A.3 the necking strains predicted by each criterion, and calculated for the power law constitutive model, are plotted against the nondimensional characteristic speed. Onset of necking results for both the sinusoidal and linear strain profiles are presented, using three values of the imperfection parameter ξ and the linearized perturbation criterion. The initial imperfection based necking curves show increasing necking strains with increasing speed. The plateau in the onset of necking with respect to deformation rate is also clear, and the influence of the linear strain profile is not pronounced according to these results. Perturbation based results show the opposite trend, i.e. a decrease of necking strain for an increase of loading rate. Note also for the linearized perturbation results that the linear loading profile shows higher necking strains than its sinusoidal counterpart, in contrast to the initial imperfection criterion.

The counterpart to the results in Fig. A.3 calculated this time for the linear overstress constitutive model are presented in Figs. A.4 and A.5. The difference in the magnitude of ϵ_{neck} for the linearized perturbation and initial imperfection criteria necessitates separate plots. A comparable stress–strain response between F_{p} and F_1 requires different $\dot{\epsilon}_0^{\mathrm{p}}$ values, giving unequal speeds $(\dot{\epsilon}_0^{\mathrm{p}}\tau_0)^{-1}$ for processes with the same forming time τ_0.
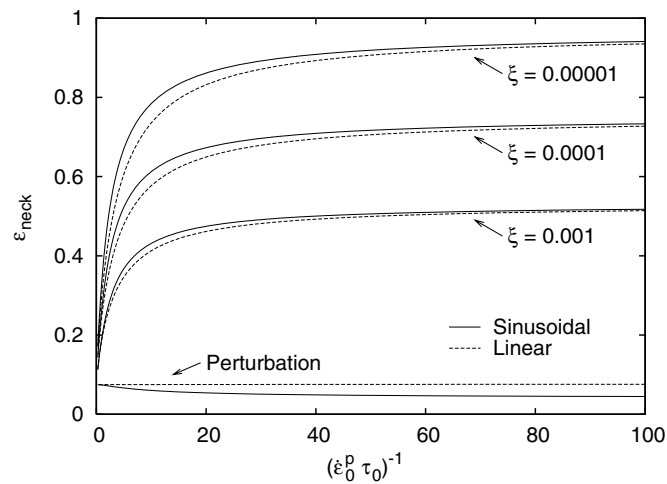

Fig. A.3. Onset of necking strain versus nondimensional strain rate based on the power law constitutive model for the sinusoidal and linear strain profiles using initial imperfection and linearized perturbation criteria.
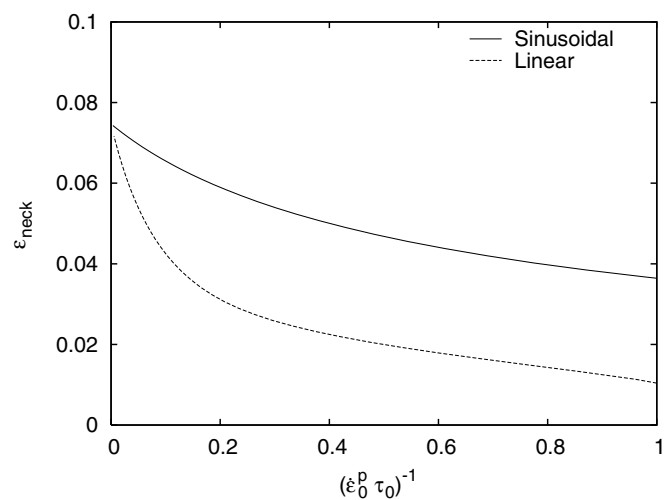

Fig. A.4. Onset of necking strain versus nondimensional strain rate using the linearized perturbation criterion and based on the linear overstress constitutive model for the sinusoidal and linear strain profiles.
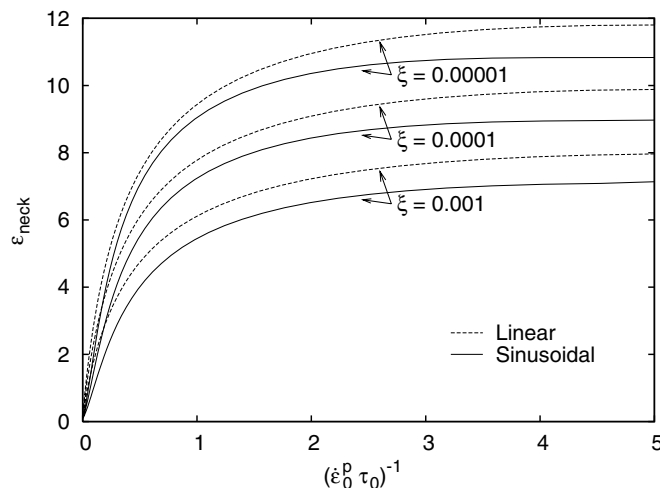
Fig. A.5. Onset of necking strain versus nondimensional strain rate using the initial imperfection criterion and based on the linear overstress constitutive model for the sinusoidal and linear strain profiles.

The strain at necking for the linearized perturbation criterion versus nondimensional loading speed is shown in Fig. A.4. Results for both the sinusoidal and linear strain profiles are shown. At quasistatic speeds the onset of necking strain approaches the quasistatic necking value (maximum force) for both strain profiles. Similarly to the results for the power law constitutive model, as $(\dot{\epsilon}_0^p \tau_0)^{-1}$ increases the linearized perturbation necking strain prediction decreases, but in contrast to the power law material (see Fig. A.3) the sinusoidal strain profile shows higher necking strains than the linear profile. Also noteworthy, the strain at necking for the linear strain profile is no longer constant with respect to forming speed.

Finally, the onset of necking strain for the initial imperfection criterion versus nondimensional characteristic speed for the sinusoidal and linear strain profiles is given in Fig. A.5. As expected for all three values of ξ, the imperfection necking strain prediction approaches the quasistatic value as $(\dot{\epsilon}_0^p \tau_0)^{-1} \to 0$, but it increases considerably at high deformation rates. For loading rates $(\dot{\epsilon}_0^p \tau_0)^{-1} > 1$ the necking stains for the linear overstress model (Fig. A.5) are rather (>4) unrealistic (and much higher than those for the power law model (Fig. A.3)). Also, unlike the power law model, the predicted necking strains with the linear overstress model for the linear strain profile are higher than those for the sinusoidal profile. However, as with the power law model, the predicted necking strains increase as ξ decreases, and there is an upper limit on the necking strains for increasing loading speed.

It is clear from the results presented above that realistic necking predictions are gained only with the initial imperfection criterion. In all the cases considered, the linearized perturbation criterion gives onset of necking strains that decrease from the quasistatic value (maximum force) monotonically with increasing loading rate. This result is in contradiction with experimental evidence from high strain rate free forming results that show formability equal to or greater than that under quasistatic conditions (see Hutchinson and Neale, 1977; Oliveira and Worswick, 2003; Hu and Daehn, 1996). The initial imperfection criterion is at this point the reasonable choice for ductility calculations of interest in this work.

References

Balanethiram, V., Daehn, G., 1992. Enhanced formability of interstitial free iron at high strain rates. Scripta Metallurgica et Materialia 27, 1783–1788.

Balanethiram, V., Daehn, G., 1994. Hyperplasticity: increased forming limits at high workpiece velocity. Scripta Metallurgica et Materialia 31, 515–520.

Barlat, F., Becker, R.C., Hayashida, Y., Maeda, Y., Yanagawa, M., Chung, K., Brem, J.C., Lege, D.J., Matsui, K., Murtha, S.J., Hattori, S., 1997a. Yielding description for solution strengthened aluminum alloys. International Journal of Plasticity 13 (4), 385–401.

Barlat, F., Maeda, Y., Chung, K., Yanagawa, M., Brem, J., Hayashida, Y., Lege, D., Matsui, K., Murtha, S., Hattori, S., Becker, R., Makosey, S., 1997b. Yield function development for aluminum alloy sheets. Journal of the Mechanics and Physics of Solids 45, 1727–1763.

Butuc, M.C., Gracio, J.J., Barata da Rocha, A., 2003. A theoretical study on forming limit diagrams prediction. Journal of Materials Processing Technology 142, 714–724.

Hill, R., 1952. On discontinuous plastic states, with special reference to localized necking in thin sheets. Journal of the Mechanics and Physics of Solids 1, 19–30.

Hutchinson, J.W., Neale, K.W., 1977. Influence of strain-rate sensitivity on necking under uniaxial tension. Acta Metallurgica 25, 839–846.

Hu, X.Y., Daehn, G.S., 1996. Effect of velocity on flow localization in tension. Acta Materialia 44 (3), 1021–1033.

Imbert, J.M., Winkler, S.L., Worswick, M.J., Oliveira, D.A., Golovashchenko, S.F., 2005. The effect of tool-sheet interaction on damage evolution in electromagnetic forming of aluminum alloy sheet. Journal of Engineering Materials and Technology-Transactions of the ASME 127, 145–153.

Krajewski, P., 2005. The warm ductility of commercial aluminum sheet alloys. Lightweight Castings and Aluminum Alloys for Advanced Automotive Applications. SAEI, Warrendale, PA.

LeRoy, G., Embury, J.D., 1978. The utilization of failure maps to compare the fracture modes occurring in aluminum alloys. In: Hecker, S.S., Ghosh, A.K., Gegel, H.L. (Eds.), Formability Analysis, Modeling, and Experimentation. AIME, New York, NY, pp. 183–207.

Marciniak, Z., Kuczynski, K., 1967. Limit strains in the processes of stretch-forming sheet metal. International Journal of Mechanical Sciences 9 (9), 609–620.

Massin, P., Triantafyllidis, N., Leroy, Y.M., 1999. On the stability of strain-rate dependent solids. I-Structural examples. Journal of the Mechanics and Physics of Solids 47 (8), 1737–1779.

Mercier, S., Molinari, A., 2004. Analysis of multiple necking in rings under rapid radial expansion. International Journal of Impact Engineering 30 (4), 403–419.

Needleman, A., Triantafyllidis, N., 1978. Void growth and local necking in biaxially stretched sheets. Journal of Engineering Materials and Technology – Transactions of the ASME 100, 164–169.

Nestorović, M.D., Leroy, Y.M., Triantafyllidis, N., 2000. On the stability of rate-dependent solids with application to the uniaxial plane strain test. Journal of the Mechanics and Physics of Solids 48, 1467–1491.

Ogawa, K., 2001. Temperature and strain rate effects on the tensile strength of 6061 aluminum alloy. In: Chiba, A., Tanimura, S., Hokamoto, K. (Eds.), Impact Engineering and Application. Elsevier Science Ltd., pp. 99–104.

Oliveira, D.A., Worswick, M.J., Finn, M., Newman, D., 2005. Electromagnetic forming of aluminum alloy sheet: Free-form and cavity fill experiments and model. Journal of Materials Processing Technology 170, 350–362.

Oliveira, D.A., Worswick, M.J., 2003. Electromagnetic forming of aluminium alloy sheet. Journal de Physique IV 110, 293–298.

Stören, S., Rice, J.R., 1975. Localized necking in thin sheet. Journal of the Mechanics and Physics of Solids 23 (6), 421–441.

Tirupataiah, Y., Sundararajan, G., 1994. The strain-rate sensitivity of flow stress and strain-hardening rate in metallic materials. Materials Science and Engineering A189, 117–127.

Triantafyllidis, N., Massin, P., Leroy, Y.M., 1997. A sufficient condition for the linear instability of strain-rate-dependent solids. Comptes Rendus de l'Academie des Sciences Series IIB Mechanics Physics Chemistry Astronomy 324 (3), 151–157.

Triantafyllidis, N., Waldenmyer, J., 2004. Onset of necking in electro-magnetically formed rings. Journal of the Mechanics and Physics of Solids 52, 2127–2148.

Yadav, S., Chichili, D., Ramesh, K., 1995. The mechanical response of a 6061-T6 A1/A12O3 metal matrix composite at high rates of deformation. Acta Metallurgica et Materialia 43, 4453–4464.

Yadav, S., Repetto, E.A., Ravichandran, G., Ortiz, M., 2001. A computational study of the influence of thermal softening on ballistic penetration in metals. International Journal of Impact Engineering 25 (8), 787–803.

Zhang, H., Ravi-Chandar, K., 2006. On the dynamics of necking and fragmentation-I. Real-time and post-mortem observations in Al 6061-O. CMSSM Report 06-05, Center for Mechanics of Solids, Structures and Materials, The University of Texas at Austin, Austin, TX.